PAPER

Check for updates

LED-driven controlled deposition of Ni onto TiO_2 for visible-light expanded conversion of carbon dioxide into C_1–C_2 alkanes†

Arturo Sanz-Marco,[ab] José L. Hueso, [ID][abc] Víctor Sebastian, [ID][abc] David Nielsen, [ID][d] Susanne Mossin, [ID][d] Juan P. Holgado, [ID][e] Carlos J. Bueno-Alejo,[ab] Francisco Balas [ID] *[abc] and Jesus Santamaria*[abc]

Photocatalytic gas-phase hydrogenation of CO_2 into alkanes was achieved over TiO_2-supported Ni nanoparticles under LED irradiation at 365 nm, 460 nm and white light. The photocatalysts were prepared using photo-assisted deposition of Ni salts under LED irradiation at 365 nm onto TiO_2 P25 nanoparticles in methanol as a hole scavenger. This procedure yielded 2 nm Ni particles decorating the surface of TiO_2 with a nickel mass content of about 2%. Before the photocatalytic runs, Ni/TiO_2 was submitted to thermal reduction at 400 °C in a 10% H_2 atmosphere which induced O-defective TiO_{2-x} substrates. The formation of oxygen vacancies, Ti^{3+} centers and metallic Ni sites upon photocatalytic CO_2 hydrogenation was confirmed by operando EPR analysis. In situ XPS under reaction conditions suggested a strong metal–support interaction and the co-existence of zero and divalent Ni states. These photoactive species enhanced the photo-assisted reduction of CO_2 below 300 °C to yield CO, CH_4 and C_2H_6 as final products.

Introduction

The overall depletion of fossil fuels and the overwhelming evidence of the impact of greenhouse gas emissions on the global environment are among the major challenges of the humankind today[1,2] and demand a swift transition to renewable and sustainable processes. Among the strategies advocated to overcome these issues are gas-phase capture and storage, and revalorization by reduction to value-added products. In particular, the catalytic hydrogenation of CO_2 for synthetic fuel production is an appealing mid-term solution to reduce the concentration of greenhouse gases, mitigate the dependence on

fossil fuels and promote an overall neutral CO_2 emission cycle.[3–7]

Photocatalysis involves a greener vision of chemical processes, including the smart and selective transformation of chemicals into fuels and/or chemical intermediates of interest.[8–10] The use of photocatalysts leads to an effective depletion of organic pollutants, either in the form of wastewater or as organic volatile compounds.[11,12] In fact, photocatalysis takes advantage of sunlight as an abundant and inexpensive energy source, providing a sustainable approach to solving the most pressing environmental issues. Alternatively, energy-efficient artificial light systems, such as light emitting diodes (hereafter LEDs) have revealed themselves as mighty allies for inducing photocatalytic processes with enhanced effectiveness (see for instance ref. 13). Current efforts are being devoted to developing novel photocatalysts that can exploit the full-solar spectrum.[14–18]

Most of the current photoactive materials are based on semiconducting oxides and heterojunctions,[19,20] where light irradiation promotes the formation of an electron–hole pair, or an exciton (e^-–h^+), in the electronic band structure of the solid, followed by the redox reaction on the surface of the catalyst. Among them, titanium dioxide, TiO_2, is the most studied photocatalytic semiconductor, due to its high photoactivity, low cost, natural abundance and non-toxicity.[21] However, its wide band gap ($E_g = 3.2$ eV for the anatase phase) limits its photoactivity to the UV region.[22,23] Some of the strategies to enhance the catalytic activity of TiO_2 involve the addition of

[a]Department of Chemical and Environmental Engineering, University of Zaragoza, c/Mariano Esquillor, s/n; Campus Rio Ebro, Edificio I+D, Zaragoza, 50018, Spain. E-mail: fbalas@unizar.es

[b]Institute of Nanoscience and Materials of Aragon (INMA), University of Zaragoza, Consejo Superior de Investigaciones Científicas (CSIC), c/Mariano Esquillor, s/n, 50018 Zaragoza, Spain

[c]Networking Research Center in Biomaterials, Bioengineering and Nanomedicine (CIBER-BBN), C/Monforte de Lemos, 3-5, 28029 Madrid, Spain

[d]Centre for Catalysis and Sustainable Chemistry, Department of Chemistry, Technical University of Denmark, Kemitorvet 207, 2800 Kgs. Lyngby, Denmark

[e]Instituto de Ciencia de Materiales de Sevilla (ICMS, CSIC-University of Seville), Avda. Americo Vespucio, s/n, Seville, 41092, Spain

† Electronic supplementary information (ESI) available: Synthesis of the nanocatalysts, analysis of the electron microscopy images, details of the operando EPR and additional catalytic activity tests. See DOI: 10.1039/d1na00021g

nanostructured co-catalysts for improving the charge separation and the catalytic kinetics[6,24] or the controlled generation of structural defects to enhance the solar absorption and the gas species adsorption on the surface.[25] Since the seminal work on TiO_2 as a heterogeneous photocatalyst,[26] there has been an outstanding development of semiconducting TiO_2-based nanostructured materials, particularly for environmental remediation applications under both liquid[27,28] and gas phase conditions.[29–31]

A wide variety of noble metal co-catalysts have been tested for the gas phase hydrogenation of CO_2 into alkanes mediated by the Sabatier's reaction in the gas phase under diverse conditions.[32–35] In addition, first-row elements have been deposited on the surface of nanosized TiO_2 under analogous conditions to develop efficient photocatalysts for numerous environmental applications.[36] Particularly, nickel on TiO_2 exhibited a high activity for the methanation reaction with dependence on the morphology, crystalline state and metal–support interactions.[37] The photo-assisted catalytic activity of Ni-containing TiO_2 catalysts has been tested, which showed that the work function of Ni lies in the appropriate range (5.3 eV) to enhance the charge separation of the TiO_2 electron bands.[38] Furthermore, Meng et al. showed that even oxidized Ni species, such as $Ni(OH)_2$, on TiO_2 nanofibers were effective for the reduction of CO_2 to methane and carbon monoxide.[39] Similarly, Ni nanoclusters on reduced TiO_2 supports have been reported to be effective for the photocatalytic conversion of CO_2 to alcohols via an aldehyde mechanism.[40] To deposit metal crystallites on TiO_2 a variety of methods have been used, including hydrothermal, co-precipitation and thermal evaporation procedures, yielding metal nanoparticles with sizes down to 10 nm on the surface of TiO_2.[41,42]

Recently, the photocatalytic nature of some semiconducting metal oxides has been leveraged to reduce metal ions to nanosized metal particles upon light irradiation.[43,44] This so-called photodeposition procedure is a liquid-phase reaction that uses light in the UV range to induce an exciton pair in the surface of TiO_2,[45] which is first trapped by surface oxygen atoms. The photogenerated holes at the Ti–OH sites act as active species for the oxidation of solvent molecules, e.g. methanol, through hydrogen evolution, and the electrons cause the reduction of metal cations present in the liquid, which precipitate as metallic particles on the surface of TiO_2.[46,47] The hole scavenging process allows a longer life of the e^-–h^+ pair and therefore a more effective metal ion reduction and deposition is achieved. Usually, the photo-assisted deposition procedure leads to metal particles, with small sizes (e.g. 5 nm), on the semiconducting oxide.[42]

In the present work, Ni-based nanosized particles have been deposited on the surface of TiO_2 nanoparticles by a photodeposition method in methanol as a hole scavenger. These materials have been successfully tested in the gas-phase photocatalytic hydrogenation of CO_2 in a fixed-bed reactor under LED irradiation at different wavelengths, including the full visible spectrum. The generation of structural defects (i.e. oxygen vacancies and Ti^{3+} defective centers) within the TiO_2 framework was investigated with operando EPR. In situ XPS

studies under reaction conditions further elucidated the coexistence of metallic and divalent Ni domains partially buried or decorating the TiO_2 support, thereby suggesting a strong metal–support interaction (SMSI). We found that the ex situ thermal pre-activation of the Ni–TiO_2 strongly promoted the light-driven/light-assisted/LED-driven CO_2 hydrogenation towards carbon monoxide, methane and ethane.

Experimental section

Synthesis of Ni–TiO_2 by LED-assisted photodeposition

A photodeposition method was used to attach Ni nanoparticles on the TiO_2 surface. Briefly, 25 mg of nanosized TiO_2 (Evonik P25, Dusseldorf, Germany) and 55 mg of nickel chloride hydrate ($NiCl_2 \cdot 6H_2O$ 98%, Sigma-Aldrich) were added to 17 ml of DI water in a 20 ml Pyrex tube, which was then closed with a rubber septum. After 20 min of degasification under nitrogen gas flow, 1 ml of methanol (CH_3OH, Sigma-Aldrich) was added to the mixture. All reagents and precursors were used without purification. The suspension was subsequently irradiated with UV light using two LED lamps (OSRAM LED Engin, Wilmington MA) at 365 nm for 270 s and under continuous magnetic stirring to induce the photocatalytic reduction of Ni salts. The so-obtained suspension was further centrifuged at 7500 rpm for 5 minutes, washed several times with a mixture of double-deionized water and ethanol, and dried at 100 °C for 10 h. The final solid samples were stored in the dark for further use and characterization. Finally, some of the samples were submitted to a gas-phase ex situ reduction procedure before characterization and photocatalytic activity tests. Typically, 150 mg of the catalyst were loaded into a ceramic crucible and placed in a tube furnace (Carbolite, Hope Valley, UK) under a 10 : 90 H_2 : N_2 atmosphere at 50 sccm and heated up to 400 °C at a 10 °C min^{-1} heating rate. The temperature was held for 2 h before cooling to room temperature under the same atmosphere. After thermal reduction, the TiO_2-based nanoparticles developed a greyish color. These nanomaterials were prepared at the Synthesis of Nanoparticles Unit 9 of the ICTS "NANBIO-SIS" at the Institute of Nanoscience of Aragon and the University of Zaragoza.

Characterization

The crystalline structures of the TiO_2 support and the photo-deposited Ni nanoparticles were identified by the X-ray diffraction (XRD) technique using a Bruker D8 Advance Diffractometer (Bruker Corporation, Billerica MA) equipped with a (002) Ge monochromator using the $CuK\alpha_1$ line at 1.5405 Å. The UV-vis spectra were recorded in a JASCO V-670 UV-vis/NIR spectrophotometer (JASCO, Tokyo, Japan) using the solid-state diffuse reflectance technique in a 60 mm UV-vis/NIR integrating sphere from 200 nm to 900 nm, with a scanning step of 10 nm s^{-1}. Temperature-programmed reduction (TPR) tests were performed in a Quantachrome ChemBET Pulsar TPR/TPD analyzer (Quantachrome Instruments, Boynton Beach, FL) equipped with a Thermal Conductivity Detector (TCD). Usually, 50 mg powdered samples were loaded in one of the branches of

a U-tube quartz reactor suspended between quartz wool pieces. Before every TPR test, samples were heated up to 100 °C under Ar gas flow to remove adsorbed species on the material surface. After cooling to room temperature, samples were heated from room temperature to 900 °C at 10 °C min^{-1} heating rate under 10 : 90 H$_2$/Ar gas flow at 20 sccm. The BET surface area and porosity of catalysts were determined by means of N$_2$ adsorption at 77 K using a Micromeritics TriStar 3000 analyzer (Micromeritics, Norcross, GA).

The TiO$_2$ P25 and Ni/TiO$_2$ were investigated by *in situ* and *operando* Electron Paramagnetic Resonance spectroscopy (EPR) on a Bruker EMX EPR instrument fitted with a ST4102 cavity and a Bruker variable temperature unit and quartz insert. The materials were pressed into pellets, then crushed and fractioned (150–300 μm). ~25 mg of sample were immobilized with quartz wool in a 4 mm inner diameter quartz tube and placed in the cavity. The EPR spectra (9.45 GHz, 20 mW, 5 Gauss modulation amplitude at 100 kHz) were continuously obtained while introducing a total gas flow of 50 Nml min^{-1} during the sample analysis. To study the influence of light irradiation, UV light pulses in 100 s intervals (Dymax Blue Wave 75) were directed *via* a glass fiber to shine on the sample tube through a grid on the side of the EPR cavity. The same experimental protocol (see the ESI†) was performed on P25 and on Ni/TiO$_2$ while monitoring with EPR to compare the responses of the photocatalysts under UV light exposure and different reaction atmospheres (see Table S1 in the ESI†). Samples were first activated in 30% H$_2$ at 250 °C. Then the influence of UV light and of the H$_2$/CO$_2$ gas (separately and together) was investigated at room temperature. Then the sample was reactivated and the procedure was repeated at 250 °C. In general, the spectra exhibited lower resolution at 250 °C, as the noise level was higher at these temperatures and the changes were more difficult to discern. Overall, the same evolution was observed, but it was less clear and thus only room temperature spectra are shown in the text. The spectrum assigned to Ni species (type 1, see the main text) changed with temperature.

The Ni metal loading was evaluated using a microwave plasma-atomic emission spectrometer (4100 MP-AES, Agilent) and X-ray photoelectron spectroscopy (XPS) spectra were obtained before and after activation using a Kratos AXIS Ultra DLD surface analysis spectrometer (Kratos Analytical Ltd., Durham, UK). *In situ* XPS studies were performed using a customized system incorporating a hemispherical analyzer (SPECS Phoibos 100), a non-monochromatized X-ray source (Al Kα; 1486.6 eV, Mg Kα, 1253.6 eV) and a high temperature–high pressure cell (SPECS-HPC-20) that allows sample heating and gas flow. The analyzer was operated at a fixed transmission and 50 eV pass energy with an energy step of 0.1 eV. Binding energies were calibrated using C 1s or Ti 2p (284.6 eV or 458.8 eV) as an internal reference. The high temperature–high pressure cell design allowed sample heating up to 800 °C, under flow or static conditions, at pressures up to 20 bar or dynamic flows in the range 20–500 Nml min^{-1}. This arrangement enabled a transfer of post-reaction samples from the reaction chamber to the spectrometer under UHV conditions, avoiding exposure to the laboratory atmosphere. Prior to each analysis, the samples were

evacuated to 10^{-9} mbar at room temperature. In a typical experiment, the sample was initially placed in the sample holder (in the form of a pelletized disc) and transferred to the spectrometer chamber where XPS spectra were acquired. The sample was then transferred under vacuum to the high-pressure cell where it was exposed to the reactive gases and heated to the appropriate temperature. The flow and concentration of gases were similar to those used for catalytic testing (*vide infra*). After the treatment the sample was cooled to room temperature under the reaction atmosphere, evacuated down to 10^{-7} mbar in less than two minutes and then transferred back to the spectrometer chamber for analysis, avoiding ambient exposure.

Aberration corrected scanning transmission electron microscopy (Cs-corrected STEM) images were acquired using a high angle annular dark field detector in an FEI XFEG TITAN electron microscope operated at 300 kV equipped with a CET-COR Cs-probe corrector from CEOS Company allowing the formation of an electron probe of 0.08 nm. The geometric aberrations of the probe-forming system were controlled to allow a beam convergence of 24.7 mrad half-angle to be selected. Elemental analysis was carried out with an EDX detector for EDS experiments in scanning mode. EDX mapping was performed with an Oxford Instruments Detector and analysed with AZtec software provided by the detector manufacturer.

Photo-assisted carbon dioxide hydrogenation tests

The CO$_2$ hydrogenation was conducted in a fixed-bed reactor as shown in Scheme 1. Typically, 120 mg of powdered catalyst was packed in a 30 × 10 × 2 mm prismatic quartz reactor that was positioned between two LED sources of different wavelengths, namely 365 nm, 460 nm and white light. Before irradiation, a gas mixture of CO$_2$ and H$_2$ with a 1 : 4 molar ratio was fed into the reactor for 30 min to ensure air removal from inside the reactor. After that, the reactor was closed and filled with the gas
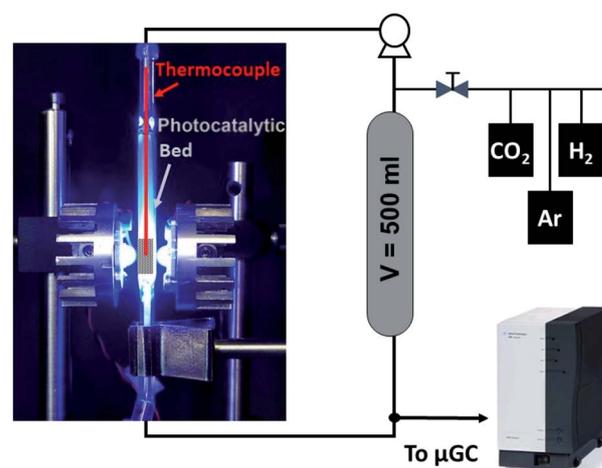
Scheme 1 Simplified flowchart of the batch reactor system used for the photocatalytic tests. Typically, the batch reactor was filled with a 25 : 75 CO$_2$/H$_2$ mixture until a P = 1.7 bar was obtained. A 15 Nml min^{-1} gas flow was recirculated through the reactor. The fixed bed was operated under 9 W LED light (4.5 W per LED). A sample of the gas mixture was analyzed by gas chromatography hourly.

mixture until an absolute pressure of 1.7 bar was reached. A recirculating OEM pump (Verderflex M1500, Groeningen, NL) caused a 7.5 ml min^{-1} gas flow through the reactor circuit that included a 500 ml chamber to buffer pressure oscillations and provide enough total volume for gas sampling in prolonged experiments. The reaction was started by turning on the LEDs, which also caused a sharp increase in the solid temperature to reach a stable value around 250 °C. A sample of the gases was periodically analyzed using an on-line 490 micro-GC analyzer (Agilent Technologies, Santa Clara, CA, equipped with three columns: a 10 m molecular sieve column with a 5 m PPQ pre-column, a 10 m PBQ column and a 10 m CP-wax). DC current was set at 0.9 A and 12 V during LED irradiation for all tested materials.

Results and discussion

Photodeposition of Ni nanoparticles on TiO$_2$ P25

The photo-assisted deposition method involves the photonic excitation of a semiconductor immersed in a solution that
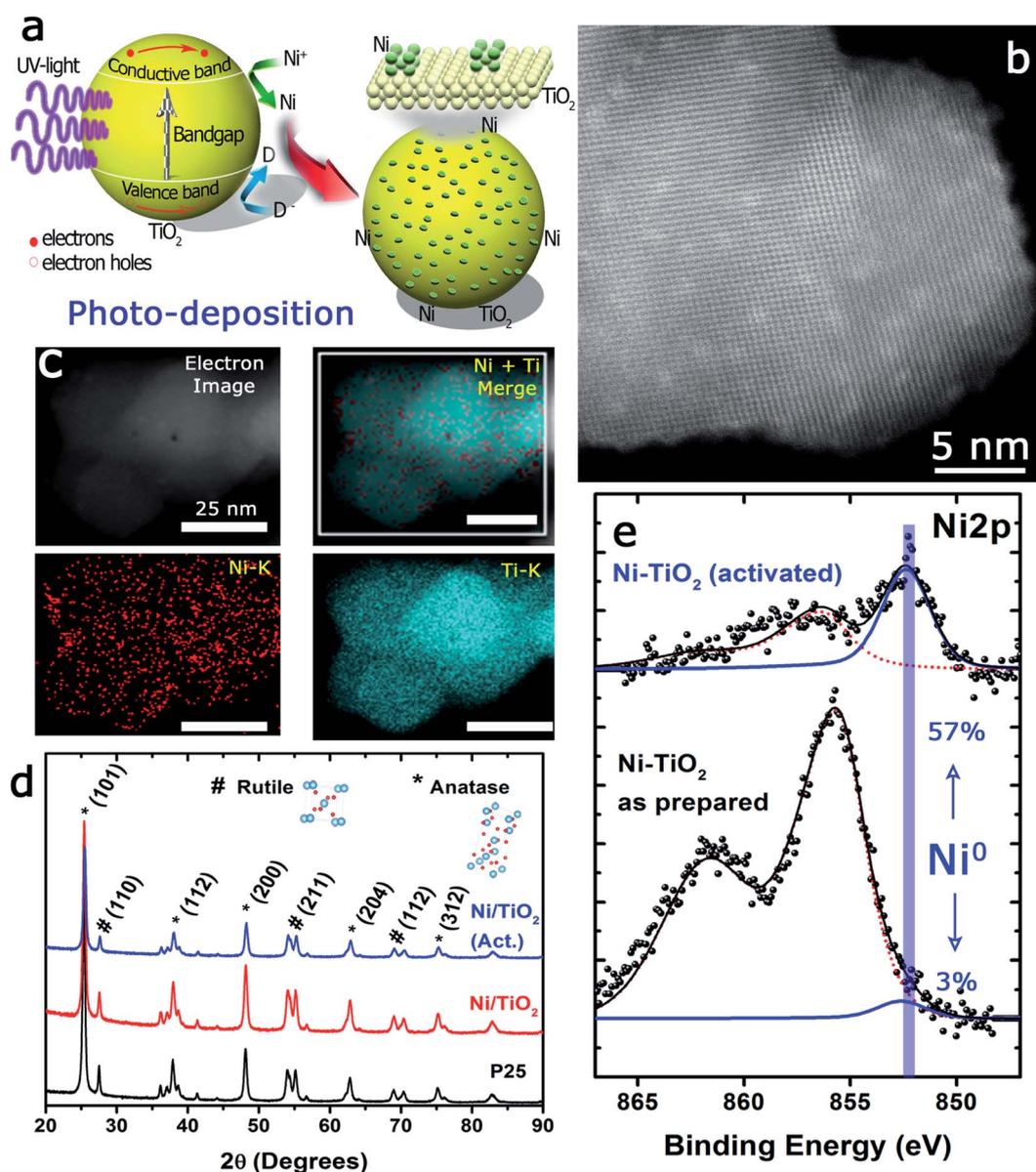

Fig. 1 Characterization of the Ni–TiO$_2$ photocatalyst: (a) scheme of the photo-assisted deposition process; (b) HAADF-STEM representative image of the Ni–TiO$_2$ photocatalyst. Dots displaying lighter contrast correspond to the small Ni domains homogeneously dispersed on the TiO$_2$ support; (c) EDX images corresponding to the selected areas shown in the inset STEM image accounting for the presence of Ti and Ni domains altogether in the catalyst nanoparticles; (d) XRD patterns of TiO$_2$ nanoparticles after photodeposition of Ni from NiCl$_2$ as the precursor and CH$_3$OH as the hole-scavenging solvent. Crystalline Ni species remained undetected and only the reflections of anatase and rutile could be found. The activation procedure at 400 °C in a 10% H$_2$ atmosphere reduced the relative height of the (100) reflection of anatase together with a slight increase in the peak width; (e) XPS spectra corresponding to the Ni 2p$_{3/2}$ region before and after activation in a reducing environment. A strong increase of reduced Ni species is observed after activation.

contains the ionic precursor of the material to be deposited and at least one liquid component that can act as a hole scavenger. When the incident photon energy is larger than the E_g, the valence band electrons can be excited to the conduction band.

The pumped electrons are therefore used for the reduction of the metallic cations in the electrolyte, Ni^{2+} in this case, to deposit nanosized metallic particles on the surface of the semiconducting oxide. To avoid fast electron–hole pair recombination or the oxidation of the photodeposited metallic particles, methanol, an easy to oxidize substrate, is used, which acts as a sacrificial agent and hole scavenger when added to the electrolyte (Fig. 1a). The photo-deposition process provided white solids with a Ni mass concentration of $1.10 \pm 0.11\%$ calculated by MP-AES spectrometry (see the Experimental section). The subsequent thermal activation at 400 °C in a 10%-H_2 atmosphere produced light grey-colored solids with a Ni mass concentration of $1.18 \pm 0.05\%$, i.e., thermal activation in the hydrogen atmosphere did not alter the Ni loading of the prepared catalysts. The Ni/TiO_2 catalyst particles exhibited similar size before and after thermal activation, between 20 and 25 nm. High-resolution HAADF-STEM images of individual Ni/TiO_2 nanostructures showed 2 nm Ni/NiO crystallites homogeneously dispersed on the TiO_2 nanoparticles (Fig. 1b). EDX analysis of individual nanoparticles confirmed the presence of Ni domains (see Fig. 1c). XRD analysis (Fig. 1d) showed the blend of anatase and rutile diffraction peaks expected for TiO_2 P25 nanoparticles, without any diffraction pattern attributable to Ni or nickel oxides. This might be attributed to the concentration of deposited Ni (<2 wt%), particularly to its extraordinary dispersion and small particle size. These 2 nm sized Ni particles could be assigned to either Ni or NiO nanoparticles. Two different chemical processes could explain the presence of NiO after photodeposition: oxidation of the deposited Ni^0 nanoparticles can take place upon environmental exposure, or the direct photodeposition of NiO particles may take place in a methanol-deficient medium.[48,49]

The UV-vis spectra showed very significant changes with respect to the absorption bands of TiO_2 P25 (Fig. 2a), which displayed a strong absorption below 400 nm corresponding to the ground excitonic state of TiO_2. The absorption bands of Ni/TiO_2 were expanded towards the visible–near infrared region resulting from the formation of either metallic Ni or NiO nanoparticles.[42,50,51] After thermal activation, the absorption in the visible region is greatly enhanced, which is due to the reducing conditions that led to the formation of oxygen vacancies and the incorporation of H-containing species or even Ti^{3+} cations on the surface of TiO_2.[52,53] Such structural modifications induced the formation of intermediate energy levels in the band gap, leading to broader light absorption.[25] Furthermore, the optical band gap estimated using the Tauc plots (Fig. 2b) returned a value of $E_g = 3.2$ eV for TiO_2, in good agreement with values reported elsewhere.[23,25] For Ni/TiO_2, a red-shift in the optical band gap could be observed which can be ascribed to an interfacial charge transfer process, consisting in the migration of electrons from the semiconducting substrate to the metallic nanoparticles directly from the valence band after excitation.[54,55] This feature was slightly more
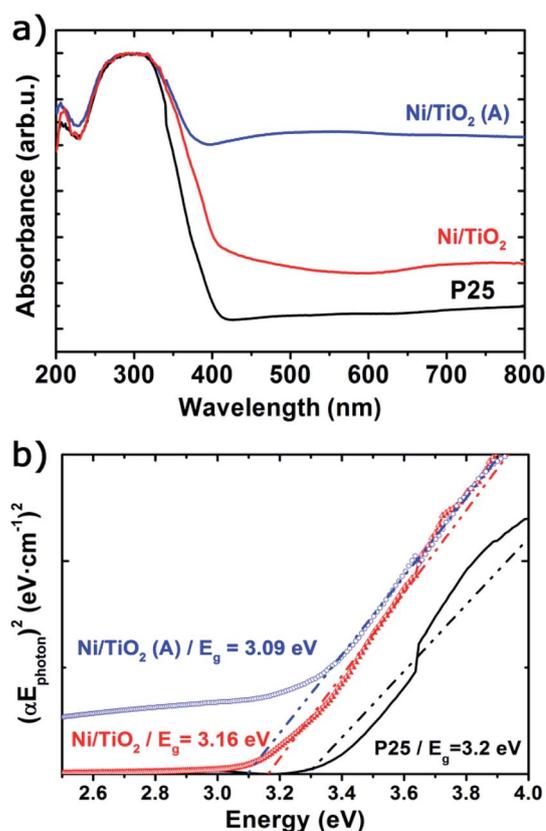

Fig. 2 UV-vis absorbance spectra (a) and Tauc plots (b) of TiO_2 before and after Ni photodeposition in MeOH/H_2O (Ni/TiO_2) and thermal activation at 400 °C in a 5%-H_2 atmosphere (Ni/TiO_2-A).

noticeable after the thermal activation in a reducing atmosphere, which could be due to the formation of O^{2-} vacancies or Ti^{3+} species on the TiO_2 surface under those conditions.[56]

The TPR tests (Fig. 3) showed that Ni^{2+}, presumably as NiO, and Ni^0 were both likely present on Ni/TiO_2 and Ni/TiO_2-A. This was concluded after the detection of reduction peaks at $T_{II} \sim 330$ °C and $T_{III} \sim 370$ °C which were attributed to the reduction of NiO species with low and high interaction with the support,
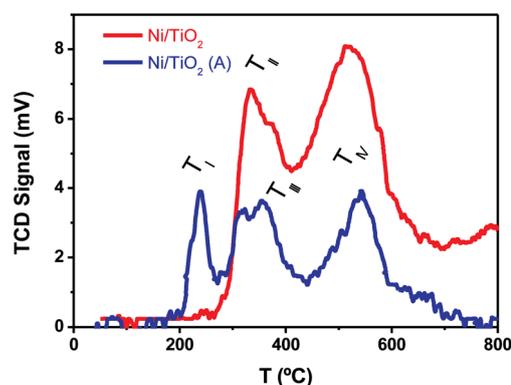

Fig. 3 TPR plots of TiO_2 before and after Ni photodeposition in MeOH/H_2O, as prepared (Ni/TiO_2), and after thermal activation at 400 °C in a 10%-H_2 atmosphere (Ni/TiO_2-A).

Table 1 Binding energies (BE, eV) and surface concentration (at%) obtained by XPS analysis for the as-prepared and activated Ni/TiO$_2$ catalysts before and after LED-assisted gas-phase photocatalytic CO$_2$ hydrogenation

BE (eV), surface concentration (at%)

	O 1s	Ti 2p	Ni 2p	C 1s
Ni/TiO$_2$	530.0	458.8	856.0	285.0
	48.99%	21.69%	3.06%	26.26%
Ni/TiO$_2$ (post-reaction)	530.3	458.3	856.3	285.3
	51.69%	20.33%	1.03%	26.94%
Ni/TiO$_2$-A	529.8	458.6	855.6	285.0
	48.50%	23.92%	0.66%	26.92%
Ni/TiO$_2$-A (post-reaction)	529.4	458.4	855.4	284.4
	51.45%	21.63%	0.14%	26.78%

respectively.[57] The signal centered at $T_{IV} \sim 550$ °C was assigned to the reduction of smaller NiO nanoparticles dispersed in the TiO$_2$ substrate with a very strong interaction.[50,58] A noticeable decrease in the signal intensities was observed for the Ni/TiO$_2$-A, which was attributed to the partial reduction of the Ni-based particles and TiO$_2$ substrate after the thermal activation in a 10%-H$_2$ atmosphere. However, the appearance of a signal at $T_I \sim 230$ °C after the activation suggested the presence of NiO particles with a weak or null interaction with the support,[58] which is in agreement with the decrease in Ni loading observed by XPS (Table 1 and Fig. S1†). This decrease in Ni loading is also observed after a photocatalytic evaluation, due to the stronger reduction atmosphere of photocatalytic tests (80%-H$_2$), which could lead to a better integration of Ni clusters within the TiO$_2$ surface.

In situ and *operando* spectroscopic studies under CO$_2$ hydrogenation conditions

With the aim of discerning the precise chemical state of the Ni and Ti on the surface of the catalyst, *operando* EPR spectroscopy has been used. Since both Ni and Ti paramagnetic centers, as well as potential ion defects, are present on the surface of the catalysts, EPR spectroscopy is undoubtedly a technique of choice.[59] For instance, Morra *et al.* have used EPR to discern the active catalytic sites in Ti-containing materials, where titanium ions could be formed in low oxidation states under diverse reaction conditions.[60]

In the present study, three different types of EPR signals were observed when performing the *in situ* and *operando* protocol. Fig. 4 shows a selection of EPR spectra and the most relevant changes observed under reaction conditions. Type 1 is observed for Ni/TiO$_2$, but not for P25 TiO$_2$. It is a huge broad peak centered at $g \sim 2.1$ (Fig. 4a), constantly present for Ni/TiO$_2$ but changes during activation, and is unaltered upon exposure to UV light. In order to follow the subtle change during activation, the spectra of the fresh sample were subtracted from the spectrum of the activated sample (Fig. 4a).

The spectral change corresponded to a broad EPR spectrum with a g-value of ~ 2.34 and a tiny sharp peak at 2.0035. The g-value of the broad signal in the difference spectrum was significantly shifted compared to the g-value of the overall spectrum (~ 2.1). Type 1 was assigned to paramagnetic Ni centers or defects in the Ni nanoparticles, which suggests the contribution from several types of Ni species, which could be either Ni^{2+} or Ni$^+$. The EPR spectrum is largely featureless for a precise assignment, but it is noted that the g-value of 2.34 for the evolved species is similar to the value observed for defect sites in pure NiO nanoparticles.[61] The type 2 signal was a small sharp isotropic signal centered at 2.0035, which was absent for the fresh materials but showed up after a few minutes and in comparable intensities for both TiO$_2$ and Ni/TiO$_2$ after activation (heating to 250 °C in 30% H$_2$). The signal of Ni/TiO$_2$-A increased during exposure to UV light (still under H$_2$), but returned back to the initial state after the light was turned off (Fig. 4b). No clear development in the signal was observed for TiO$_2$ during interaction with UV light (data not shown). The signal is not influenced by either of the materials being exposed to the H$_2$/CO$_2$ gas mixture. The type 2 signal was assigned to sites in the bulk of the nanoparticles: either an F-center, an electron caught in an oxygen vacancy, or a V-center, an oxygen ion caught at a cation vacancy.[62,63]

Finally, type 3 was a small anisotropic signal centered at 2.011 which is visible only for Ni/TiO$_2$-A. It overlapped with the type 1 signal and was barely influenced by exposure to UV light; however, it disappeared completely after exposure to the H$_2$/CO$_2$ mixture (notice the negative change in the spectrum in Fig. 4b). It was tentatively assigned to oxygen-centered surface hole trapping sites in the anatase polymorph of TiO$_2$ P25.[64] The anisotropy of the signal is due to the direction dependence of surface sites. This type of site is observed in the literature on pure TiO$_2$ at low temperatures (<100 K) where the signal to noise ratio of EPR is much better. In our catalyst such evidence suggests that the introduction of very small Ni particles by photodeposition has promoted the number of these sites to the extent that they are now observable by EPR at room temperature and above. The fact that they are sensitive to the H$_2$/CO$_2$ mixture confirms the assignment as surface sites and is an indication that they are involved directly in the reaction of CO$_2$ on the surface of the material.

The state of Ni species on the TiO$_2$ substrates was further explored using XPS analysis (Fig. 4c and Table 1). It is interesting to note that the XPS signals corresponding to the Ni 2p levels were rather complex, being deconvoluted up to three Gaussian/Lorentzian peaks (see the ESI, Table S2 and Fig. S1†). This situation is typically found in the presence of multiplet contributions and satellite structures, whose formation could be found in recent papers.[50,65] For Ni^{2+} the satellite at about +6.0 eV might be assigned to a final state effect associated with a (core) 3d^{8}L configuration (where L stands for ligands). However, the intensity and position of this satellite depended on many factors such as bonding with ligands, symmetry, particle size and crystallinity.[66,67]

Furthermore, a noticeable decrease of the atomic concentration of Ni was observed after thermal activation under a H$_2$ atmosphere at 400 °C (Table 1). This might be attributed to the process of Ni nanoparticle growth by sintering or, alternatively, to an incomplete immersion of the Ni particles into the support
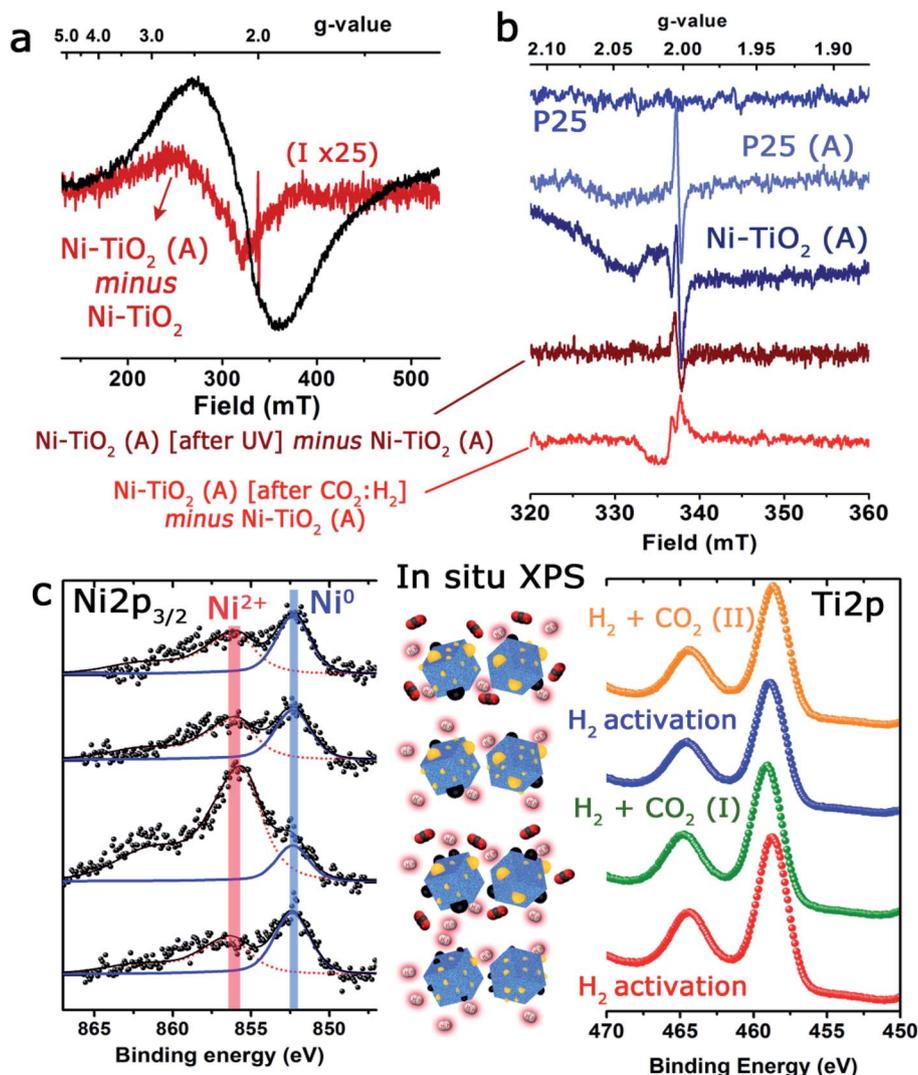
Fig. 4 *In situ* and *operando* spectroscopic studies under a CO_2 hydrogenation reaction environment: (a) selected X-band EPR spectra collected at room temperature of TiO_2 and Ni/TiO_2 before and after thermal activation at 250 °C in 30% H_2 and of Ni/TiO_2-A before and after exposure to UV light and H_2/CO_2 at room temperature; full spectrum of Ni/TiO_2 (black) and change in the EPR spectrum (×25) upon activation (red). (b) Zoom-in of the EPR spectra of TiO_2 before (blue) and after activation (light blue), Ni/TiO_2 after activation (dark blue) and the change after exposure to UV-light (brown) and after exposure to $H_2 + CO_2$ (light red); (c) XPS spectra corresponding to the Ni $2p_{3/2}$ and the Ti 2p regions after submitting the catalyst sample to successive thermal treatments for either the reduction/activation (10 vol% H_2–Ar; flow rate: 20 Nml min^{-1}; 400–450 °C) or carbon dioxide hydrogenation reaction ($CO_2 : H_2 - 1 : 4$; flow rate: 5 Nml min^{-1}; 60 mg of pelletized 1.2 wt% Ni/P25 photocatalyst; 225 °C).

due to the "decoration" effect of the TiO_2 over the Ni particles. This has been previously reported for a variety of metal catalysts on different supports,[68] within the context of the strong metal–support interaction (SMSI) effect.[69] Both events would be enhanced in the case of nanosized particles[70,71] and under treatment with hydrogen. In addition, the absence of complete reduction of Ni particles (only 57% of Ni^0 after the reduction treatment) would also support this hypothesis.

In situ XPS observations were carried out to evaluate the evolution of the oxidation states of Ni and Ti under activation or CO_2 hydrogenation conditions at 225 °C giving interesting and complementary insights into the *operando* EPR results. Although the change of the oxidation state of Ti was unclear

(Fig. 4c), after the initial CO_2/H_2 treatment, an incomplete recovery of Ni signal intensity and a notable oxidation of the particles were noticed (Ni^{2+} concentration about 84%). These facts would be in agreement with the expected behavior in a SMSI scenario, with the CO_2 serving as a mild re-oxidation agent. After the second reduction treatment at 450 °C, the situation was similar to that described before, and a decrease in intensity and a partial reduction of the Ni particles were noticed (Fig. 4c and Table S3†).

Nevertheless, after the second treatment with the CO_2/H_2 mixture, neither the Ni signal intensity nor the Ni^{2+}/Ni^0 ratios were remarkably altered. This could reflect a more permanent coverage of the Ni particles caused by the reduction at a higher

temperature under hydrogen and would reinforce the close interaction between Ni and TiO_2 as suggested by EPR. Actually, the HAADF-STEM images of the catalysts after reaction revealed that while a fraction of Ni domains have coarsened, the majority of the catalyst maintained similar particle size distributions (see Fig. S2†).

Light-assisted gas-phase photocatalytic CO_2 hydrogenation

The photocatalytic conversion of CO_2 into CO, CH_4 and C_2H_6 alkanes was observed under LED irradiation at different wavelengths (Fig. 5). The photocatalytic performance of TiO_2 P25 under UV light was evaluated before Ni photodeposition (see Fig. S4a†). Also, a control experiment was carried using Ni/TiO_2 under 365 nm LED irradiation in 4/1 Ar/H_2 stream. No CO, CH_4 or C_2H_6 signals were detected after reaction for 6 h (Fig. S4b†). Results showed CO productivity around 100 μmol g_{cat}^{-1} h^{-1} during the 6 h of reaction time. The signals attributed to both CH_4 and C_2H_6 were also detected, at concentrations below the quantification limit. In contrast, when Ni/TiO_2 catalysts were illuminated at 365 nm (Fig. 5a), the main product obtained was CH_4 with a maximum initial productivity of 450 μmol g_{cat}^{-1} h^{-1} and an increased CO productivity of 250 μmol g_{cat}^{-1} h^{-1}. Also, the production of C_2H_6 remained almost constant during the reaction, reaching about 2 μmol g_{cat}^{-1} h^{-1}. Catalyst activation by the high temperature hydrogen treatment produced two main effects: first, the photocatalytic activity increased significantly under UV light (Fig. 5b), and second, the catalytic response is expanded to the visible region of the solar spectrum (Fig. 5c and d). This increase in the CO and C_2H_6 (~4 μmol g_{cat}^{-1} h^{-1}) productivity under UV light for the Ni/TiO_2-A could be attributed to the formation of both bulk and surface oxygen

vacancies (V_O) on the TiO_2 phase upon hydrogenation and the enhancement of the SMSI effect as suggested by the *in situ* XPS data. These V_O induced donor intermediate energy levels in the bandgap, which might act as electron traps, facilitating charge-carrier separation and charge transfer to the adsorbed species. The irradiation under UV LEDs was more effective for the generation of CO. A similar trend with lower productivity was also found for the Ni/TiO_2-A under LED illumination at blue light (460 nm, Fig. 5c) and white light (Fig. 5d). Interestingly, similar catalytic activity tests under blue or white LED irradiation using the as-synthesized Ni/TiO_2 catalysts before thermal activation showed CO productivity lower than 25 μmol g_{cat}^{-1} h^{-1} up to 4 h of reaction (data not shown).

The temperature at the center of the fixed bed during the reaction was about 250 °C when 460 nm and white LED units were used, but increased to 270 °C and 300 °C for the Ni–TiO_2 and Ni/TiO_2-A under UV illumination, respectively, which could simply be a result of a higher absorbance of the catalyst at 365 nm, but may also reflect the contribution of plasmonic effects in the Ni/NiO nanoparticles located at the surface of the TiO_2,[72,73] as recent studies have shown that plasmonic nanoparticles deposited on TiO_2 could act as nanoheaters on the surface of the semiconductor.[74]

The photothermal CO_2 hydrogenation is expected to proceed through the exothermic Sabatier reaction ($CO_2 + 4H_2 \rightarrow CH_4 + 2H_2O$, $\Delta H^0 = -165$ kJ mol^{-1}).[75] Alternatively, for TiO_2-based materials the reverse water gas shift (RWGS) reaction has also been proposed, yielding CO and water vapor ($CO_2 + H_2 \rightarrow CO + H_2O$, $\Delta H^0 = 41$ kJ mol^{-1}).[74] It has been suggested that these reactions could occur through the dissociation of physisorbed CO_2 into CO intermediates that either evolve to formate[76] or to
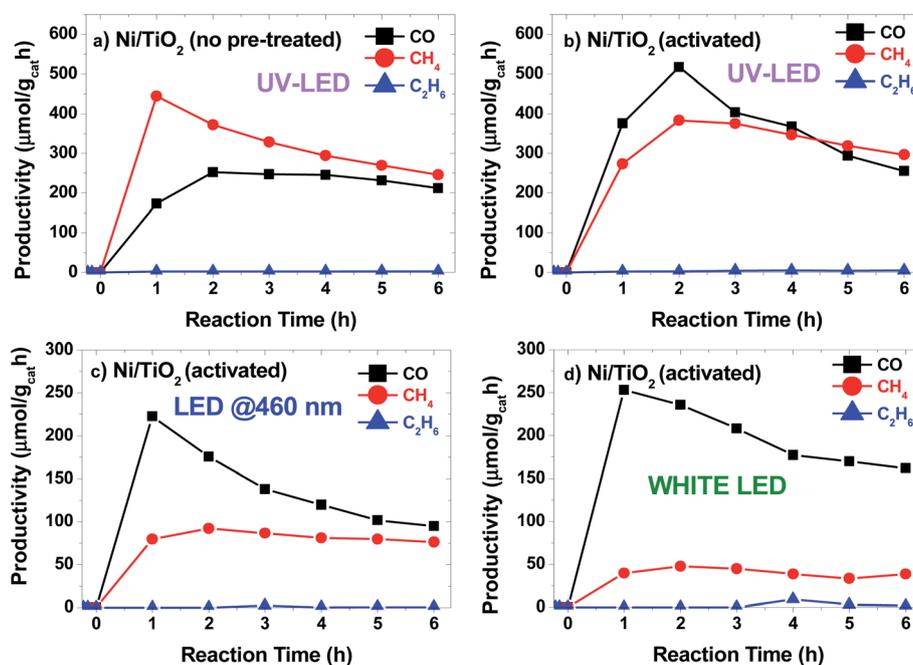

Fig. 5 Productivity *vs.* time plots for Ni/TiO_2 catalysts (a) under LED light irradiation at 365 nm and for Ni/TiO_2-A catalysts under LED irradiation at 365 nm (b), 460 nm (c) and white light (d).
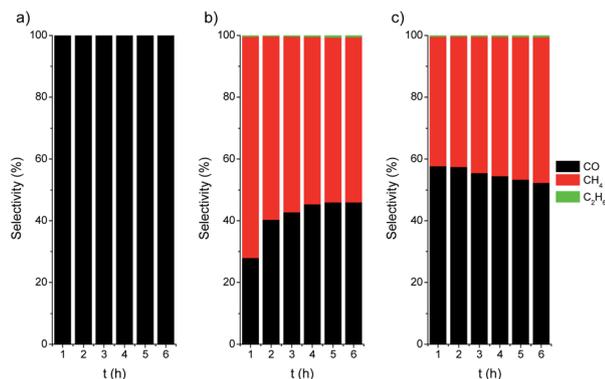
Fig. 6 Selectivity *vs.* time plots for TiO_2 P25 (a), Ni/TiO_2 (b) and Ni/TiO_2-A (c) catalysts under UV LED irradiation (365 nm).

carbide to finally form CH_4 molecules upon further hydrogenation.[77] In our case the CO_2 hydrogenation progressed to the formation of CH_4 on active centers, namely Ni/NiO nanoclusters, followed to a certain extent by a C–C coupling up to the formation of C_2H_6. At this point, it should be noted that the direct formation of ethane from CO_2 over Ni was reported to be very minimal.[78] On the other hand, the C–C coupling in the gas phase to generate higher hydrocarbons, such as ethane, over Ni-based catalysts was recently reported to be independent of the structure and only controlled by the hydrogenation rate.[79] The photo-assisted deposition of Ni was critical for the CO hydrogenation to alkanes (Fig. 6). For Ni-containing catalysts, the initial selectivity to CH_4 is close to 70%, decreasing down to 60% after 6 h of catalytic test. After activation (Ni/TiO_2-A), the selectivity slightly evolved towards CH_4, which can be attributed to an increase in the SMSI after the reduction treatment.

Finally, the thermally activated catalysts (Ni/TiO_2-A) also exhibited a higher production of both C_2 and C_1 alkanes. In this case, the formed V_O in the TiO_2 could act as centers for the enhanced adsorption of CO_2, thus improving the hydrogenation rate. The oxygen-defective TiO_2 also induced the formation of Ti^{3+} species (see TPR data in Fig. 3), which have been reported to have a photonic response upon illumination with UV photons.[25,80,81] These combined effects resulted in enhanced conversion of CO_2 even under illumination in the visible range.

Conclusions

Ni/NiO nanosized particles were effectively deposited on the surface of TiO_2 nanoparticles by a photodeposition procedure that used Ni^{2+} salts as precursors and CH_3OH as a hole scavenger. The synthesis of very small Ni crystallites on TiO_2 was achieved under the irradiation of LEDs at 365 nm. A thermal activation under a reducing atmosphere allowed the stabilization of Ni^0 on the catalyst surface, as well as the formation of oxygen vacancies that could enhance the CO_2 adsorption.

Under LED illumination at different wavelengths, the Ni/TiO_2 catalysts induced the photocatalytic hydrogenation of CO_2 at 300 °C to produce CO, CH_4 and C_2H_6 with a productivity of about 450 μmol g_{cat}^{-1} h. The thermally reduced catalysts (Ni/

TiO_2-A) showed enhanced photocatalytic response in the UV region and higher CO productivities in all the studied wavelengths. As the thermal reduction induces the formation of active sites in the TiO_2 support, the RWGS reaction is favored, increasing the CO selectivity. Further EPR and XPS analyses suggested that the close interaction of the metal and support plays an important role in the enhancement of photoactivity.

Conflicts of interest

There are no conflicts to declare.

Acknowledgements

References

1 IEA, *World Energy Outlook 2018*, IEA, Paris, 2018, https://doi.org/10.1787/weo-2018-en.

2 BP p.l.c., *BP Energy Outlook*, 2019.

3 K. Li, X. An, K. H. Park, M. Khraisheh and J. Tang, *Catal. Today*, 2014, **224**, 3–12.

4 P. R. Yaashikaa, P. Senthil Kumar, S. J. Varjani and A. Saravanan, *J. CO₂ Util.*, 2019, **33**, 131–147.

5 L. Wang, M. Ghoussoub, H. Wang, Y. Shao, W. Sun, A. A. Tountas, T. E. Wood, H. Li, J. Y. Y. Loh, Y. Dong, M. Xia, Y. Li, S. Wang, J. Jia, C. Qiu, C. Qian, N. P. Kherani, L. He, X. Zhang and G. A. Ozin, *Joule*, 2018, **2**, 1369–1381.

6 Y. Wang, J. Zhao, Y. Li and C. Wang, *Appl. Catal., B*, 2018, **226**, 544–553.

7 F. Zhang, Y. H. Li, M. Y. Qi, Z. R. Tang and Y. J. Xu, *Appl. Catal., B*, 2020, **268**, 118380.

8 X. Liu, X. Duan, W. Wei, S. Wang and B. J. Ni, *Green Chem.*, 2019, **21**, 4266–4289.

9 Q. Mu, W. Zhu, X. Li, C. Zhang, Y. Su, Y. Lian, P. Qi, Z. Deng, D. Zhang, S. Wang, X. Zhu and Y. Peng, *Appl. Catal., B*, 2020, **262**, 118144.

10 F. Xu, J. Zhang, B. Zhu, J. Yu and J. Xu, *Appl. Catal., B*, 2018, **230**, 194–202.

11 O. Tursunov, L. Kustov and A. Kustov, *Oil Gas Sci. Technol.*, 2017, **72**, 30.

12 X. Li, J. Yu, M. Jaroniec and X. Chen, *Chem. Rev.*, 2019, **119**, 3962–4179.

13 C. J. Bueno-Alejo, J. L. Hueso, R. Mallada, I. Julian and J. Santamaria, *Chem. Eng. J.*, 2018, **358**, 1363–1370.

14 C. Zhang, H. Q. Liang, Z. K. Xu and Z. Wang, *Adv. Sci.*, 2019, **6**, 1900883.

15 R. P. Ye, J. Ding, W. Gong, M. D. Argyle, Q. Zhong, Y. Wang, C. K. Russell, Z. Xu, A. G. Russell, Q. Li, M. Fan and Y. G. Yao, *Nat. Commun.*, 2019, **10**, 5698.

16 Y. Liu, C. Miao, P. Yang, Y. He, J. Feng and D. Li, *Appl. Catal., B*, 2019, **244**, 919–930.

17 S. Zhu, X. Chen, Z. Li, X. Ye, Y. Liu, Y. Chen, L. Yang, M. Chen, D. Zhang, G. Li and H. Li, *Appl. Catal., B*, 2020, **264**, 118515.

18 X. Feng, F. Pan, H. Zhao, W. Deng, P. Zhang, H. C. Zhou and Y. Li, *Appl. Catal., B*, 2018, **238**, 274–283.

19 X. Yu, T. J. Marks and A. Facchetti, *Nat. Mater.*, 2016, **15**, 383–396.

20 M. Liras, M. Barawi and V. A. De La Peña O'Shea, *Chem. Soc. Rev.*, 2019, **48**, 5454–5487.

21 A. Dhakshinamoorthy, S. Navalon, A. Corma and H. Garcia, *Energy Environ. Sci.*, 2012, **5**, 9217–9233.

22 B. Wang, S. Shen and S. S. Mao, *J. Mater.*, 2017, **3**, 96–111.

23 Y. Liu, L. Tian, X. Tan, X. Li and X. Chen, *Sci. Bull.*, 2017, **62**, 431–441.

24 M. C. Ortega-Liebana, J. L. Hueso, S. Ferdousi, R. Arenal, S. Irusta, K. L. Yeung and J. Santamaria, *Appl. Catal., B*, 2017, **218**, 68–79.

25 J. Jia, C. Qian, Y. Dong, Y. F. Li, H. Wang, M. Ghoussoub, K. T. Butler, A. Walsh and G. A. Ozin, *Chem. Soc. Rev.*, 2017, **46**, 4631–4644.

26 K. Nakata and A. Fujishima, *J. Photochem. Photobiol. C Photochem. Rev.*, 2012, **13**, 169–189.

27 U. I. Gaya and A. H. Abdullah, *J. Photochem. Photobiol. C Photochem. Rev.*, 2008, **9**, 1–12.

28 J. C. Colmenares and R. Luque, *Chem. Soc. Rev.*, 2014, **43**, 765–778.

29 C. J. Bueno-Alejo, J. L. Hueso, R. Mallada, I. Julian and J. Santamaria, *Chem. Eng. J.*, 2019, **358**, 1363–1370.

30 W. Bi, Y. Hu, N. Jiang, L. Zhang, H. Jiang, X. Zhao, C. Wang and C. Li, *Appl. Catal., B*, 2020, **269**, 118810.

31 Z. Deng, J. Ji, M. Xing and J. Zhang, *Nanoscale Adv.*, 2020, **2**, 4986.

32 J. Xu, X. Su, H. Duan, B. Hou, Q. Lin, X. Liu, X. Pan, G. Pei, H. Geng, Y. Huang and T. Zhang, *J. Catal.*, 2016, **333**, 227–237.

33 A. Karelovic and P. Ruiz, *J. Catal.*, 2013, **301**, 141–153.

34 A. Petala and P. Panagiotopoulou, *Appl. Catal., B*, 2018, **224**, 919–927.

35 C. Vogt, M. Monai, G. J. Kramer and B. M. Weckhuysen, *Nat. Catal.*, 2019, **2**, 188–197.

36 K. E. Dalle, J. Warnan, J. J. Leung, B. Reuillard, I. S. Karmel and E. Reisner, *Chem. Rev.*, 2019, **119**, 2752–2875.

37 R. Zhou, N. Rui, Z. Fan and C. J. Liu, *Int. J. Hydrogen Energy*, 2016, **41**, 22017–22025.

38 B. S. Kwak, K. Vignesh, N. K. Park, H. J. Ryu, J. I. Baek and M. Kang, *Fuel*, 2015, **143**, 570–576.

39 A. Meng, S. Wu, B. Cheng, J. Yu and J. Xu, *J. Mater. Chem. A*, 2018, **6**, 4729–4736.

40 T. Billo, F.-Y. Fu, P. Raghunath, I. Shown, W.-F. Chen, H.-T. Lien, T.-H. Shen, J.-F. Lee, T.-S. Chan, K.-Y. Huang, C.-I. Wu, M. C. Lin, J.-S. Hwang, C.-H. Lee, L.-C. Chen and K.-H. Chen, *Small*, 2018, **14**, 1702928.

41 W. T. Chen, A. Chan, D. Sun-Waterhouse, T. Moriga, H. Idriss and G. I. N. Waterhouse, *J. Catal.*, 2015, **326**, 43–53.

42 W. T. Chen, A. Chan, D. Sun-Waterhouse, J. Llorca, H. Idriss and G. I. N. Waterhouse, *J. Catal.*, 2018, **367**, 27–42.

43 Y. Lee, E. Kim, Y. Park, J. Kim, W. H. Ryu, J. Rho and K. Kim, *J. Mater.*, 2018, **4**, 83–94.

44 K. Wenderich and G. Mul, *Chem. Rev.*, 2016, **116**, 14587–14619.

45 S. Dadsetan, S. Baghshahi, F. Farshidfar and S. M. M. Hadavi, *Ceram. Int.*, 2017, **43**, 9322–9326.

46 J. L. Rodríguez, M. A. Valenzuela, F. Pola, H. Tiznado and T. Poznyak, *J. Mol. Catal. A: Chem.*, 2012, **353–354**, 29–36.

47 A. Y. Ahmed, T. A. Kandiel, I. Ivanova and D. Bahnemann, *Appl. Surf. Sci.*, 2014, **319**, 44–49.

48 V. Iliev, D. Tomova, L. Bilyarska and G. Tyuliev, *J. Mol. Catal. A: Chem.*, 2007, **263**, 32–38.

49 A. Mills and M. A. Valenzuela, *J. Photochem. Photobiol., A*, 2004, **165**, 25–34.

50 C. J. Bueno-Alejo, A. Arca-Ramos, J. L. Hueso and J. Santamaría, *Catal. Today*, 2020, **355**, 678–684.

51 H. Yang, Z. Jin, K. Fan, D. D. Liu and G. Lu, *Superlattices Microstruct.*, 2017, **111**, 687–695.

52 X. Jiang, Y. Zhang, J. Jiang, Y. Rong, Y. Wang, Y. Wu and C. Pan, *J. Phys. Chem. C*, 2012, **116**, 22619–22624.

53 Y. Guo, L. Xiao, M. Zhang, Q. Li and J. Yang, *Appl. Surf. Sci.*, 2018, **208**, 432–439.

54 K. Fujiwara, K. Okuyama and S. E. Pratsinis, *Environ. Sci.: Nano*, 2017, **4**, 2076–2092.

55 H. Irie, S. Miura, K. Kamiya and K. Hashimoto, *Chem. Phys. Lett.*, 2008, **457**, 202–205.

56 S. Wei, R. Wu, X. Xu, J. Jian, H. Wang and Y. Sun, *Chem. Eng. J.*, 2016, **299**, 120–125.

57 X. Lin, L. Lin, K. Huang, X. Chen, W. Dai and X. Fu, *Appl. Catal., B*, 2015, **168–169**, 416–422.

58 W. Lin, H. Cheng, L. He, Y. Yu and F. Zhao, *J. Catal.*, 2013, **303**, 110–116.

59 S. Van Doorslaer and D. M. Murphy, EPR Spectroscopy in Catalysis, in *EPR Spectrosc. Appl. Chem. Biol.*, ed. M. Drescher and G. Jeschke, Springer, Berlin, Heidelberg, 2012, pp. 1–39.

60 E. Morra, E. Giamello and M. Chiesa, *J. Magn. Reson.*, 2017, **280**, 89–102.

61 M. Hashem, E. Saion, N. M. Al-Hada, H. M. Kamari, A. H. Shaari, Z. A. Talib, S. B. Paiman and M. A. Kamarudeen, *Results Phys.*, 2016, **6**, 1024–1030.

62 A. Naldoni, M. Altomare, G. Zoppellaro, N. Liu, Š. Kment, R. Zbořil and P. Schmuki, *ACS Catal.*, 2019, **9**, 345–364.

63 T. Jia, J. Zhang, J. Wu, D. Wang, Q. Liu, Y. Qi, B. Hu, P. He, W. Pan and X. Qi, *Mater. Lett.*, 2010, **265**, 127465.

64 D. C. Hurum, A. G. Agrios, K. A. Gray, T. Rajh and M. C. Thurnauer, *J. Phys. Chem. B*, 2003, **107**, 4545–4549.

65 M. C. Biesinger, B. P. Payne, A. P. Grosvenor, L. W. M. Lau, A. R. Gerson and R. S. C. Smart, *Appl. Surf. Sci.*, 2011, **257**, 2717–2730.

66 V. Biju and M. Abdul Khadar, *J. Nanopart. Res.*, 2002, **4**, 247–253.

67 N. S. McIntyre, D. D. Johnston, L. L. Coatsworth, R. D. Davidson and J. R. Brown, *Surf. Interface Anal.*, 1990, **15**, 265–272.

68 L. E. Oi, M. Y. Choo, H. V. Lee, H. C. Ong, S. B. A. Hamid and J. C. Juan, *RSC Adv.*, 2016, **6**, 108741–108754.

69 Z. Xu, Y. Li, J. Zhang, L. Chang, R. Zhou and Z. Duan, *Appl. Catal., A*, 2001, **210**, 45–53.

70 A. Caballero, J. P. Holgado, V. M. Gonzalez-De la Cruz, S. E. Habas, T. Herranz and M. Salmeron, *Chem. Commun.*, 2010, **46**, 1097–1099.

71 V. M. Gonzalez-De la Cruz, J. P. Holgado, R. Pereñíguez and A. Caballero, *J. Catal.*, 2008, **257**, 307–314.

72 R. Wang, Y. Li, R. Shi and M. Yang, *J. Mol. Catal. A: Chem.*, 2011, **344**, 122–127.

73 J. Zhao, B. Liu, L. Meng, S. He, R. Yuan, Y. Hou, Z. Ding, H. Lin, Z. Zhang, X. Wang and J. Long, *Appl. Catal., B*, 2019, **256**, 117823.

74 L. B. Hoch, P. G. O'Brien, A. Jelle, A. Sandhel, D. D. Perovic, C. A. Mims and G. A. Ozin, *ACS Nano*, 2016, **10**, 9017–9025.

75 K. Stangeland, D. Kalai, H. Li and Z. Yu, *Energy Procedia*, 2017, 2022–2027.

76 C. Heine, B. A. J. Lechner, H. Bluhm and M. Salmeron, *J. Am. Chem. Soc.*, 2016, **138**, 13246–13252.

77 C. Vogt, E. Groeneveld, G. Kamsma, M. Nachtegaal, L. Lu, C. J. Kiely, P. H. Berben, F. Meirer and B. M. Weckhuysen, *Nat. Catal.*, 2018, **1**, 127–134.

78 S. Abelló, C. Berrueco and D. Montané, *Fuel*, 2013, **113**, 598–609.

79 C. Vogt, M. Monai, E. B. Sterk, J. Palle, A. E. M. Melcherts, B. Zijlstra, E. Groeneveld, P. H. Berben, J. M. Boereboom, E. J. M. Hensen, F. Meirer, I. A. W. Filot and B. M. Weckhuysen, *Nat. Commun.*, 2019, **10**, 1–10.

80 E. Lira, S. Wendt, P. Huo, J. Ø. Hansen, R. Streber, S. Porsgaard, Y. Wei, R. Bechstein, E. Lægsgaard and F. Besenbacher, *J. Am. Chem. Soc.*, 2011, **133**, 6529–6532.

81 J. Ye, J. He, S. Wang, X. Zhou, Y. Zhang, G. Liu and Y. Yang, *Sep. Purif. Technol.*, 2019, **220**, 8–15.